WILEY-VCH

Tailoring antiferromagnetic orders and spin transport in noncollinear Mn_3Pt multilayers

Shaohai Chen[1]†, Bee Chun Lim[1]†, Dennis J. X. Lin[1]†, Jian Rui Soh[2], Hui Ru Tan[1], Hang Khume Tan[1], Hnin Yu Yu Ko[1], Seng Kai Wong[1], Mingsheng Zhang[1], Robert Laskowski[3], Tieyang Zhao[4], Jingsheng Chen[4], Khoong Hong Khoo[3], Pin Ho[1]**
† denotes equal author contributions

S. C., B. C. L., D. J. X. L., H. R. T., H. K. T., H. Y. Y. K., S. K.W., M. Z., P. H.
Institute of Materials Research & Engineering (IMRE), Agency for Science, Technology and Research (A*STAR), 138634, Singapore
E-mail: chensh1@imre.a-star.edu.sg; hopin@imre.a-star.edu.sg

J. R. S.
Quantum Innovation Centre (Q.InC), Agency for Science, Technology and Research (A*STAR),138634, Singapore

R. L., K. H. K.
Institute of High Performance Computing (IHPC), Agency for Science, Technology and Research (A*STAR), 138632, Singapore

T. Z., J. C.
Department of Material Science and Engineering, National University of Singapore, 117551 Singapore

Keywords: Noncollinear, Antiferromagnetic, Mn_3Pt, Anomalous Hall Effect, DFT

Abstract: Noncollinear antiferromagnetic (NCAF) materials, such as Mn_3Pt, exhibit remarkable spin-orbit and tunnelling phenomena, positioning them as promising candidates for low-power, stray-field immune nanoelectronics. However, precise control of AF order and spin transport properties, and understanding of their physical mechanisms, remains challenging. In this work, we establish the interplay between crystal structure, magnetic orders, and anomalous Hall effect (AHE) in single-crystalline Mn_3Pt (001) synthesized from a $[Mn/Pt]_{20}$ multilayer with tunable Mn layer thickness (t_{Mn}). Resonant elastic x-ray scattering reveals a magnetic ordering transition at ~240 K for the sample with t_{Mn} = 0.7 nm, which notably coincides with an AHE polarity reversal occurring around 230 K. Importantly, we demonstrate that T_c can be precisely engineered by fine-tuning t_{Mn} to modulate lattice constant and spin canting. Further, first principles calculations affirm the lattice parameter and spin canting-dependence of AHE from the ground-state Γ_{10} magnetic symmetry. Finally, a refined analytical model is introduced to elucidate the intrinsic and extrinsic AHE contributions in NCAF material comprising hybrid magnetic orders. These findings provide a robust framework for tailoring transport properties towards the realization of next-generation AF computing technologies.

1. Introduction

Noncollinear antiferromagnetic (NCAF) materials with magnetic and electronic chirality have garnered significant attention for their unique physical phenomena, enabling promising scalable and low-power electronic applications[1-3] Among them, Kagome NCAF materials – such as Mn_3X (X = Pt, Ir, Rh, Sn, Ge, Ga), feature magnetic atoms arranged in a Kagome lattice, stabilized by a complex interplay between magnetic exchange, geometric frustration and plausibly longer-range exchange couplings, and exhibiting a characteristic 120° triangular spin configuration.[4-8] Due to the nonvanishing Berry curvature and nontrivial band topology, these Kagome NCAF materials exhibit intriguing properties such as magnetoelectrically manipulable non-zero magnetization and detectable large anomalous Hall effect (AHE).[9-20] Additionally, recent theoretical and experimental studies reveal that NCAF Mn_3X (X = Sn, Ir, Pt) [21, 22] and their doped counterparts Mn_3YN (Y = Pt, Sn, Ga, Ni)[23] can achieve large spin polarization comparable to that of traditional ferromagnetic (FM) materials, enabling high tunnelling magnetoresistance (TMR) ratios in NCAF-based magnetic tunnel junctions. Within the Mn_3X family of compounds, Mn_3Pt in particular is a well-poised candidate for next-generation ultralow power electronics, due to its large ambient TMR ratios exceeding 100%,[22, 24] ultrafast tetra-hertz spin dynamics that can be driven electrically via spin torque,[25-27] and high spin orbit torque efficiency for working as spin source.[28-30]

In this vein, the development of highly chemically ordered Mn_3Pt thin films with tunable properties is sought-after for bespoke memory and computing devices. Lattice strain, crystalline texture and crystal structure modifications arising from different growth conditions can modulate the Mn_3Pt NCAF characteristics, evident from the spectrum of reported anomalous Hall conductivity (σ) ranging from 2 – 74 $\Omega^{-1}cm^{-1}$.[10, 31, 32] However, an approach to precisely manipulate the crystal structure of Mn_3Pt structure so as to control the NCAF characteristics, including AHE, has not been established thus far. Additionally, AHE contributions arising from the different NCAF magnetic orders, spin-canting induced FM components, and temperature-induced collinear AF order transition at higher device operation temperatures, have not been clearly elucidated.[31, 33-36] Crucially, current analytical methods assume an AF magnetic order model to explain the origin of AHE in NCAF, but neglect a rigorous consideration of other symmetry-allowed magnetic orders.[37] Hence, a refinement of the scaling law accounting for the complex and dynamic magnetic behaviors is imperative.

Here, we systematically examine the composition and temperature dependence of the crystal and magnetic structure of chemically ordered Mn_3Pt, and how the associated NCAF magnetic order is intricately correlated with the spin transport properties. First, our Mn_3Pt thin films were synthesized via an unprecedented $[Mn/Pt]_n$ multilayer stacking technique, enabling precise control over the Mn layer thickness (t_{Mn}=0.6−0.8 nm). Second, the temperature evolution of the magnetic order in the Mn_3Pt multilayers was characterized by resonant elastic x-ray scattering (REXS) and spin transport measurements, revealing the presence of a magnetic order transition which is associated with a polarity reversal of the sign of AHE. In line with density functional calculations,[38, 39] the observed trend of decreasing transition temperatures with increasing Mn thickness is attributed to lattice constant c variation and spin canting. Third, we introduced complementary AF and FM scaling laws to describe the underlying mechanisms of the AHE intrinsic and extrinsic contributions arising from changing c and spin canting. Our work provides a means of modulating the interplaying structural, magnetic, and electronic transport properties in NCAF Mn_3Pt, paving the development of emerging AF computing applications.

2 Results and Discussion

2.1 Epitaxial Growth of (001) Ordered Mn_3Pt Film

The Mn:Pt stoichiometry presents an important tuning knob for modulating the NCAF crystal structures, magnetic orders and emergent spin transport features. To effectively control the elemental composition of the Mn_3Pt, we adopt a Mn/Pt multilayer growth technique consisting of varying Mn thickness. Here, multilayer stacks comprising 20-repeats of [Mn (t_{Mn} = 0.6 – 0.8 nm) / Pt (0.1 nm)] (norminal thickness in nm in parenthesis) are sputter-deposited on single-crystalline MgO (100) substrates at a substrate temperature of 500 °C, followed by natural cooling under high vacuum condition to assist strain relaxation (**Figure 1a**, Methods). The Mn/Pt layer stoichiometry of our stacks is found to range between $Mn_{2.4}Pt$ and $Mn_{3.2}Pt$ (SI **Figure S1**). The samples exhibit granular surface morphology, with the root-mean-square roughness (R_q) increasing from 1.45 to 3.36 nm as the t_{Mn} increases (SI Figure S2). This indicates that the Mn_3Pt films grow predominantly via an island-like (Volmer-Weber) growth mode. Based on the Mn-Pt stoichiometry-temperature phase diagram,[40] we expect our Mn_3Pt layer in our thin films to crystallize with the Cu_3Au-type ($L1_2$) crystal structure, with the Kagome planes stacked along the [111] direction of the cubic lattice (**Figure 1b**).[33-35]

Indeed, the x-ray diffraction (XRD) patterns show the characteristic (001) and (002) structural peaks at 2θ positions of ~23° and 47.5°, affirming the presence of chemically ordered NCAF Mn_3Pt thin films across the entire range of t_{Mn} (**Figure 1c**). Specifically, the emergence of the (001) reflection indicates the formation of a chemically ordered $L1_2$-type Mn_3Pt structure, consistent with Cu_3Au-type alloys.[33] Meanwhile, we find a lattice parameter c of 3.80 ± 0.03 Å from our thin films (SI Table S1), which is compatible with previous studies.[31-34] Furthermore, we found that increasing t_{Mn} (up to 0.75 nm) leads to a reduction of the size of the cell parameter c from 3.83 to 3.78 Å (Figure 1c, SI Table S1). Beyond which at t_{Mn}: 0.8 nm, the excessive Mn content results in the relaxation of c. This expansion is attributed to the incorporation of excess Mn atoms into the Pt substitutional sites or interstitial positions,[41] which introduces structural disorder and degrades overall crystallinity. Additionally, the (001) and (002) structural peak of the Mn_3Pt film with t_{Mn} = 0.7 nm displays the lowest full width at half maximum (FWHM) (SI Table S2), hence exhibiting the highest degree of crystalline chemical ordering. Subsequent analysis would henceforth focus on the thickness range of t_{Mn}: 0.6 – 0.75 nm.

The cross-sectional transmission electron microscopy (TEM) and fast fourier transform (FFT) patterns were acquired for the representative t_{Mn} = 0.7 nm sample to study the effect of the substrate on the crystal structure of the Mn_3Pt layer. High-resolution TEM shows clear lattice fringes of the Mn_3Pt film and MgO, suggesting excellent epitaxial growth and crystallinity of the Mn_3Pt film. The scanning TEM (**Figure 1d**, left inset) reveals the ordered distribution of Mn and Pt atoms within the crystal lattice, consistent with the XRD results (Figure 1b) comprising of stacked Kagome layers. Meanwhile, the reciprocal space map (Figure 1d, right top) shows lattice constants a (and b) and c of 4.0 and 3.8 Å, respectively, wherein c corroborates well with the XRD calculations. Compared to the ideal $L1_2$ Mn_3Pt lattice constants of $a = b = c = 3.71$ Å, the larger a (7.8%) for the multilayer film suggests that the MgO substrate (a = 4.2 Å, Figure 1d, right bottom) induces a tensile strain at the MgO/Mn_3Pt interface, resulting in the Kagome lattice distortion with the expansion of the a (and b) and corresponding reduction in c. [31, 42]

2.2 Magnetic ordering of NCAF Mn_3Pt Material

Theoretical and experimental neutron diffraction studies have established the existence of a first-order transition temperature (T_1 ~ 365K), below the Néel temperature (T_N ~ 475K), for single-crystalline Mn_3Pt.[33-35] The magnetic structure exhibits a collinear AF phase above T_1 and transitions to a NCAF phase below T_1. Two NCAF magnetic structures have been proposed thus far to account for the magnetic phase below T_1. The first is where the Mn magnetic moments align head-to-tail in the Kagome plane (**Figure 2a**), whereas the second is where the magnetic moments align in a head-to-head or tail-to-tail configuration (**Figure 2b**). Even though these two magnetic structures are seemingly related under a 90° rotation of the Mn magnetic moments within the Kagome plane, they are symmetry distinct and belong to the Γ_7 and Γ_{10} irreducible magnetic structures, respectively.[43-45]

Based on our group theory analysis for Mn magnetic moments residing at the 3*c* Wyckoff position of the cubic $Pm\bar{3}m$ (#221) space group, we found that the Γ_7 and Γ_{10} magnetic structures are the only symmetry allowed magnetic configurations for temperatures below T_1. The Γ_7 symmetry describes all the magnetic structures which can be composed of three AF basis vectors ($\boldsymbol{\psi}_1$, $\boldsymbol{\psi}_2$, $\boldsymbol{\psi}_3$) (Figure 2a, right). Crucially, the magnetic structure which possess Γ_7 symmetry is always compensated, which precludes the formation of a net FM component and generation of AHE. In contrast, the magnetic structures with Γ_{10} symmetry constitute basis vectors with FM order ($\boldsymbol{\psi'}_1$, $\boldsymbol{\psi'}_2$, $\boldsymbol{\psi'}_3$, $\boldsymbol{\psi'}_4$, $\boldsymbol{\psi'}_5$, $\boldsymbol{\psi'}_6$) (Figure 2b, right) and thus is expected to generate a non-zero AHE. A case example of the general magnetic orderings which transform with Γ_7 and Γ_{10} symmetry is described by constructing their net magnetic moments using the linear combination – $M(\Gamma_7) \propto (\boldsymbol{\psi}_1 + \boldsymbol{\psi}_2 + \boldsymbol{\psi}_3)$ and $M(\Gamma_{10}) \propto (-\boldsymbol{\psi'}_1 - \boldsymbol{\psi'}_2 - \boldsymbol{\psi'}_3 + 2\boldsymbol{\psi'}_4 + 2\boldsymbol{\psi'}_5 + 2\boldsymbol{\psi'}_6)$ (SI Table S3). Meanwhile, the magnetic moments of the collinear AF stabilized in the temperature range $T_1 \leq T \leq T_N$ possess Γ_7 symmetry and can be described by $\boldsymbol{M} \propto \boldsymbol{\psi}_1$, which also leads to diminished AHE.

To determine the magnetic and crystal structure changes of the Mn sublattice as a function of measurement temperature (T_m), we performed REXS measurements on the Mn_3Pt multilayer with t_{Mn} = 0.7 nm. **Figure 2c** shows the intensity of the Mn_3Pt (001) peak as a function of the incident photon energy at T_m = 300 K. The energy dependence reveals a resonant peak at the Mn *K* edge (E ~ 6.55 keV, red), which results from resonant enhancement due to the ordering of the Mn magnetic sublattice. **Figure 2d** plots the T_m-dependence of the intensity of the Mn_3Pt (001) reflection with the incident photon energies on (E = 6.55 keV) and off (E = 6.52 eV) the Mn *K* edge resonance, which are sensitive to the magnetic and crystal structure respectively. We observe that the intensity of the structural reflection (blue curve) is invariant as a function of T_m while the intensity of the magnetic peak (red curve) increases gradually followed by a distinct dip at T_m ~ 240 K. The former confirms that the structural texture remains unchanged over the T_m range, while the latter indicates a reorganization of magnetic ordering around ~240 K. However, given that both the Γ_7 and Γ_{10} magnetic structures produce magnetic intensity on the (001) reflection, the REXS measurements cannot differentiate the magnetic structures at different T_m.

2.3 Crystalline and Magnetic Structure Variation at Different T_m

To explore the correlation between the NCAF Mn_3Pt magnetic structures and ordering with their spin transport properties, AHE measurements were performed on the Hall bar devices (**Figure 3b** inset; Methods M2) consisting of t_{Mn} = 0.6 – 0.75 nm across varying T_m = 150 – 400 K. Upon the removal of the ordinary Hall contribution from the raw data (SI **Figure S4**), we obtain the anomalous Hall resistivity (ρ_{AHE}) versus external magnetic field ($\mu_0 H$) loops (AHE loops) for these Hall bars. The negative slope of the ordinary Hall effect background indicates that electrons are the dominant carriers in our Mn_3Pt system. For correlated studies with the REXS experiments, we first examine the Hall bar device consisting of t_{Mn} = 0.7 nm (**Figure 3a,**

b). With a measured longitudinal Hall resistivity (ρ_{xx}) of 245 μΩ·cm at 300 K (SI Figure 4aS8c), the anomalous Hall conductivity ($|\sigma_{AHE}|$) at room temperature (RT) is determined to be $|\frac{\rho_{AHE}}{\rho_{xx}{}^2}|$ = 0.017 $(\Omega\cdot cm)^{-1}$. Both the ρ_{xx} and σ_{AHE} values are comparable with the reported values from epitaxially growth Mn_3Pt film.[31, 36] There is also no discernible hump-like features, suggesting the absence of topological Hall effect contributions. The magnetic hysteresis loop similarly shows no step-like features, indicating coherent magnetization switching, albeit with smaller coercive fields compared to AHE loops attributed to different field- vs electric-induced origins (SI S1). Intriguingly, the AHE loops show a flip in polarity with T_m variation i.e., $T_m \geq 250$ K and ≤ 200 K shows positive and negative polarity, respectively (Figure 3a). Here, the positive (counterclockwise) and negative (clockwise) polarity corresponds to the positive and negative ρ_{AHE}^{ZF} of the AHE loops, respectively.[46] A closer examination of the T_m-dependence of remanent ρ_{AHE} (ρ_{AHE}^{ZF}, marked in Figure 3a), following saturation at $\mu_0 H = +8$T, shows that the AHE loop switches from negative to positive polarity at a critical temperature (T_c) of ~230 K (Figure 3b).[47] Meanwhile, the magnitude of $|\rho_{AHE}^{ZF}|$ gradually increases with an increasing deviation of T_m from T_c. Such spin transport characteristics are consistent with the REXS observations of rearrangement of magnetic orders at ~240 K and stability of different magnetic orders at $T_m >> T_c$ or $T_m << T_c$. Additionally, the ρ_{AHE}^{ZF} shows non-zero value at $T_m \geq 350$ K which starkly differs from reported AHE behaviours in epitaxial (001)-textured Mn_3Pt, wherein a negative AHE loop is sustained across T_m = 10 – 345 K followed by a plunge to zero at $T_m > T_1 \approx 350$K. [31]

Figure 3c shows the normalized AHE loops of the t_{Mn} = 0.6 – 0.75 nm devices at T_m = 300K. The RT AHE loop changes from negative to positive polarity at $t_{Mn} \geq 0.7$ nm. While early work reported single polarity RT AHE loops across varying compositions in (001)-textured $Mn_{2.62\text{-}5.25}Pt$ films,[42] the dichotomy in polarity of our AHE loops may be ascribed to the multilayer growth technique and compositional deviation of our $Mn_{2.4\text{-}2.5}Pt$ (t_{Mn} = 0.6 – 0.75 nm) devices from reported. **Figure 3d** summarizes the variation of T_c and $|\sigma_{AHE}|$ as a function of t_{Mn} for T_m = 350 K (AHE loops shown in SI **Figure S5**). For the t_{Mn} = 0.6 nm device, the negative AHE loop is no longer observed at ~350 K and is marked by a near-zero $|\sigma_{AHE}|$ at $T_m \geq 350$ K (open circles), consistent with the transition behaviors at T_1. Meanwhile, for devices with $t_{Mn} \geq$ 0.65 nm, the T_c decreases from 325 to 200 K and they exhibit non-zero $|\sigma_{AHE}|$ at $T_m \geq 350$K.

In this vein, we posit that the T_m and t_{Mn} dependence of AHE are built upon the interplaying effects of magnetic structures and orderings. On one hand, the NCAF Γ_{10} magnetic structure, consisting of FM basis vectors, provides the negative polarity AHE signatures (**Figure 3e**). On the other, variations in T_m and t_{Mn} alter the magnetic ordering of the NCAF Γ_{10} magnetic structure, triggering the reversal to positive AHE polarity. Notably, the t_{Mn} = 0.6 nm device with the largest *c* conserves the ideal NCAF in-Kagome plane magnetic ordering, hence exhibiting the AHE loops with negative polarity (yellow region) over $T_m \leq 300$ K. At $T_m > T_1 \sim 350$ K, the transition to a collinear AF structure ($\boldsymbol{M} \propto \boldsymbol{\psi_1}$) gives rise to vanishing AHE signal (blue area), along with a rapid suppression of magnetization (SI Figure S3-1). Meanwhile, for devices with $t_{Mn} \geq 0.65$ nm of reduced *c*, a new magnetic order ground state generates a FM component to the NCAF Γ_{10} magnetic ordering. This FM ordering contributes to positive AHE polarity and becomes increasingly stable at higher T_m with more extensive lattice distortion (purple area). Such lattice distortion-induced AHE polarity changes may be ascribed to variations in the intrinsic, e.g. Fermi level shifts [10, 47], and extrinsic scattering, e.g. spin canting contributions to AHE [37]. Notably, experimental validation of the spin canting effect in (001)-textured Mn_3Pt is non-trivial.[36] In the next two sections, we elucidate the origin of lattice distortion-induced AHE variation using density functional theory calculations and collective AF and FM scaling laws. In our theoretical models, Mn substitution of the Pt lattice sites was not considered as there is no over-doping of Mn beyond the Mn_3Pt stoichiometric ratio of 3:1 (SI Figure S1).

2.4 DFT Contribution

First, we utilized first principles density functional theory (DFT) calculations to investigate the influence of lattice constant variations on the stability of the Mn_3Pt materials under Γ_7 and Γ_{10} magnetic structures (Methods, SI Figure S6). The calculated magnetic anisotropy energies were fitted to the form of $K\sin^2\theta$, where K and θ are the anisotropy constant and spin rotation angle in the Kagome plane from Γ_{10} to Γ_7 states (inset of **Figure 4a**). For an ideal $L1_2$ Mn_3Pt crystal with equivalent lattice constants $a = b = c$, increasing the lattice constant c from 3.79 to 4.0 Å leads to a discernible reduction in K from 3.77 to 0.3 meV per unit cell (Figure 4a, dotted lines). The decreasing K with increasing lattice constant indicates that the relative stability of the Γ_7 and Γ_{10} magnetic structure can be effectively modulated by adjusting the lattice parameters of the Mn_3Pt crystal structure. Further calculations in close reference to our fabricated Mn_3Pt multilayers with lattice constant $a = b$ (= 4.0 Å) and c (= 3.78 – 3.83 Å) suggest a smaller K difference between the Γ_7 and Γ_{10}, in contrast to the former scenario, albeit Γ_{10} remains more energetically stable than Γ_7 magnetic structure (Figure 4a, solid lines).

Combining DFT eigenfunctions and eigenvalues with a Wannier interpolation scheme, we correspondingly calculated the AHC (σ) of Mn_3Pt as a function of Fermi energy shift.[48, 49] **Figure 4b** presents the AHC contributions from the crystallographic (111)-planes, σ_{111} (schematic in SI **Figure S6a**), of the Γ_7 and Γ_{10} magnetic structure with c = 3.80 Å and across varying c = 3.78 – 3.83 Å, respectively. The calculations show that the Mn_3Pt Γ_7 magnetic structure does not contribute to AHC (Figure 4b, SI **Figure S6b**), corroborating with symmetry analysis in Section 3. In contrast, the Γ_{10} magnetic structure is the main source of AHE, yielding a non-zero σ_{111} with a magnitude of 34~67 Ω^{-1} cm^{-1} at zero Fermi energy shift (Figure 4b). These findings are consistent with literature, affirming that only the Γ_{10} magnetic order generates a finite AHC when spin-orbit coupling is present [9, 28] affirming that only the Γ_{10} magnetic order generates a finite AHC when spin-orbit coupling is present. Notably, the calculated σ_{111} exhibit qualitatively consistent positive sign convention across changing c, suggesting additional contributing factors to the experimental AHE polarity reversal beyond crystal lattice compression or expansion. Quantitatively, it is difficult to directly compare the theoretical and experimental σ values, as the DFT calculations do not account for factors such as crystal structure distribution, thermal fluctuations and extrinsic scattering induced by impurities.[5]

Henceforth, we explore the variation in the σ_{111} of the system when the spin orientation tilts out of the Kagome plane for the representative case of c = 3.80 and 3.82 Å (corresponding to the t_{Mn} = 0.7 and 0.65 nm multilayer). For these cases, the projections of the spins onto the Kagome plane maintain the same 120° separation as in the ground Γ_{10} state (inset of Figure 4c). The calculations reveal that with the spin tilt angle (Φ) exceeding 5°, the σ_{111} transitions sharply from positive to negative (**Figure 4c**). Further, σ_{111} remains in the negative regime up till as high as Φ = 15 °. In line with theoretical validation, we posit that the reversal of AHE loop from negative to positive polarity for the t_{Mn}: 0.65 – 0.75 nm multilayers when $T_m > T_c$ arises due to spin canting effects. Beyond t_{Mn}: 0.65 nm, the increasing compression of c of the Mn_3Pt lattice induces a stronger out-of-plane moment tilt, shifting the T_c away from the T_1 as the lattice deviates from the collinear AF order.

2.5 Origins of AHE

Given the complexity of magnetic orders in $L1_2$ Mn_3Pt, a singular conventional AF or FM model is insufficient to depict the AHE phenomenology in its entirety. Rather than validating the fitting models solely based on estimates of the longitudinal conductivity[50,51], we adopt a two-pronged AF[37] and FM[52] universal scaling law approach to examine the physical origin of AHE for the NCAF multilayer devices of t_{Mn} = 0.6 ~0.75 nm. For the negative polarity AHE loops exhibiting predominantly NCAF magnetic order, the data were fitted to the universal AF scaling law[37], defined as

$$\rho_{AHE} = \boldsymbol{a'}\rho_{xx,T} + \boldsymbol{b'}\rho_{xx,T}^2 \quad (1)$$

where ***a'*** and ***b'*** describes the contributions from extrinsic skew scattering and intrinsic scattering, respectively, while the $\rho_{xx,T}$ is the longitudinal Hall resistivity at different T_m. Meanwhile, the positive polarity AHE loops comprising AF Γ_{10} magnetic structure with out-of-plane FM components, is fitted with the universal FM scaling law[52] to explore contributions from spin canting effects, defined as

$$\rho_{AHE} = \boldsymbol{\alpha}\rho_{xx,0} + \boldsymbol{\beta}\rho_{xx,T} + \boldsymbol{b'}\rho_{xx,T}^2 \quad (2)$$

wherein $\boldsymbol{\alpha}$ and $\boldsymbol{\beta}$ describes the role of defects and phonons, respectively, in the extrinsic skew scattering (and side jump) process, while ***b'*** similarly describes the intrinsic scattering contribution. The $\rho_{xx,0}$, i.e. $\rho_{xx,T}$ at 0K, is obtained from the *x*-intercept of the linear fitted $\rho_{xx,T}$ versus T_m plot (SI Figure S8, Table S4). Crucially, the ***b'*** value obtained in the AF scaling law fitting is incorporated within the fitting analysis of the FM scaling law for a comprehensive understanding of AF and FM contributions in chemically ordered Mn_3Pt. (Detailed fitting procedures are shown in SI **Figure S9**)

In **Figure 5a**, we present the variation of parameters ***a'*** and ***b'*** derived from the AF scaling law for t_{Mn} = 0.6 - 0.75 nm Mn_3Pt multilayer films. Consistent with previous reports,[37] the fitting results show that ***a'*** and ***b'*** exhibit negative and positive signs across all samples, respectively. Based on the negative ρ_{AHE}^{ZF} and positive $\rho_{xx,T}$ values used in the fitting, it can be inferred that the negative ***a'*** determines the negative AHE polarity. Meanwhile, the magnitude of both $|\boldsymbol{a'}|$ and $|\boldsymbol{b'}|$ increase nearly linearly with increasing t_{Mn}. The ~71% and ~132% enhancement in $|\boldsymbol{a'}|$ and $|\boldsymbol{b'}|$, respectively, is primarily attributed to the increased FM spin tilting effect associated with a reduction of the lattice constant *c*. Additionally, the significant higher increase of $|\boldsymbol{b'}|$ with increasing t_{Mn} may be ascribed to the augmented overall thickness of the Mn_3Pt layer, thereby reducing interfacial scattering and improving intrinsic scattering.[37, 47]

By fitting the t_{Mn} = 0.65 ~0.75 nm Mn_3Pt multilayer films using the FM scaling law, $\boldsymbol{\alpha}$ exhibit enhanced positive values, while $\boldsymbol{\beta}$ show relatively larger negative values with increasing t_{Mn} (**Figure 5b**). These suggest that, in Mn_3Pt multilayer lattice with spin tilting, the extrinsic contribution of phonons to the AHE signal dominates that of defects, and the contributions of the two has opposing sign convention. Meanwhile, given the positive ρ_{AHE}^{ZF} and $\rho_{xx,T}$ values used in the fitting, this indicates that the negative phonon contribution weakens the total AHE signal. For the enhanced $|\boldsymbol{\alpha}|$ and $|\boldsymbol{\beta}|$, this can be attributed to the increased roughness of the samples with increasing t_{Mn} (SI Figure S2), which leads to higher contributions from defects and impurities.[51]

3. Conclusion

Our study systematically investigates the tuning of crystal structure, magnetic orders and spin transport properties in NCAF Mn_3Pt films through the precise control of composition and temperature. Utilizing a multilayer $[Mn/Pt]_{20}$, the Mn layer thickness is finely tuned to modulate the lattice constant and out-of-plane spin tilting, enabling control over the critical temperature associated with AHE polarity reversal. By combining experimental REXS observations with theoretical symmetry analysis and DFT calculations, our work highlights the dominant role of the Γ_{10} magnetic structure in contributing to AHE, which is highly sensitive to lattice distortions of the crystal structure and out-of-plane spin tilting of the magnetic structure. Furthermore, an unprecedented refinement of the scaling framework disentangles intrinsic and extrinsic AHE contributions, offering deeper insights into the interplay between crystal structure and magnetic ordering of NCAF.

NCAF materials with magnetic and electronic chirality have gained immense research traction for their distinctive physical manifestations, such as large anomalous Hall effect (AHE),[10, 12, 13, 31] efficient spin current generation in an applied electric field (spin Hall

effect)[29, 30, 53, 54] or thermal gradient (Nernst effect)[55-58], magneto-optical effects and magnon excitation[59-62] – despite the absence of net magnetization. Here, the highly crystalline and tunable Mn_3Pt multilayer thin films established in this work opens exciting possibility for tailored AF-based memory and computing technologies. First, we posit that future studies of tunable magnetic structures on an extended array of NCAF materials systems could benefit from harnessing their unique symmetry-allowed magnetic orders and magnetoelectric interaction mechanisms. Crucially, the realization of NCAF Mn_3Pt multilayer with tunable magnetic structures and spin transport characteristics prompt immediate employment along technological lines, especially within perpendicular magnetic tunnel junction devices. The demonstrable modulation of FM and AF components using lattice constant and temperature variations enables mechanistic investigations towards concomitant low-power electrical switching and high frequency dynamics while retaining large detection signal,[18, 22, 25, 63-65] Finally, their robustness to external field perturbation and negligible stray field effects are well suited for highly scalable, field-immune computing applications such as in multistate random access memory and synaptic computing.[66, 67] Importantly, besides spintronics, NCAF materials will open new avenue for applications in topological electronics, energy harvesting, optics and magnon-based communications.[5]

4. Experimental Section/Methods

Multilayer Films. The thin films consisting of single-crystal MgO (001) substrate/Mn_3Pt (14 – 18 nm) were fabricated using the Chiron™ magnetron physical vapor sputtering system with a base pressure of < 1 x 10^{-8} Torr. The Mn_3Pt layer was formed by depositing 20 repetitions of [Mn (t_{Mn}: 0.6 – 0.8 nm) / Pt (0.1 nm)] bilayers at the substrate temperature of 500°C. A Ta (5 nm) capping layer was subsequently deposited at RT on the Mn_3Pt layer to avoid surface oxidation and complex Mn-O texture formation. All layer thickness indicated here correspond to nominal thickness in nm. Due to the active Mn vaporization during high temperature deposition, 2-3 times more Mn content is deposited to compensate for the significant loss of Mn during deposition. The final Mn/Pt layer stoichiometry is determined to be $Mn_{2.4\text{-}3.2}Pt$ (SI Figure S1) from the atomic concentration depth profile analysis using the AXIS Supra+™ x-ray photoelectron spectroscopy tool.

Device Fabrication. A 300 nm thick negative resist, Ma-N 2403, was spin-coated on the multilayer film. Hall bar devices of dimensions width (w) × length (l) = 10 × 60 μm were exposed using the Elionix™ electron beam lithography tool. The patterns were transferred onto the multilayer film using the Oxford CAIBE™ ion beam etching system, and residual resist was lifted off in an ultrasonic bath.

Crystal structure Characterization. The x-ray diffraction (XRD) θ-2θ scans were performed using Bruker™ D8 Discoverer with Cu K_α (1.54 Å) radiation to determine the crystallographic texture and degree of crystallinity of the Mn_3Pt multilayer thin film. In addition, cross-sectional transmission electron microscopy (TEM) lamella of the $[Mn\ 0.7/Pt\ 0.1]_{20}$ sample was prepared by focused ion beam milling (FEI™ Helios Nanolab 600). Atomic resolution high-angle annular dark-field scanning transmission electron microscopy (HAADF-STEM) imaging was performed using the spherical aberration-corrected TEM (Thermo Scientific™ Spectra TEM), operating at 300 kV in STEM mode.

Morphology and Magnetic Property Characterization. The atomic force microscopy (AFM) measurements were performed on the t_{Mn} = 0.6- 0.8 nm samples using the DI 3100 SPM at room temperature. The out-of-plane magnetic hysteresis loops were measured by a Quantum Design™ superconducting quantum interference device (SQUID) system on the t_{Mn} = 0.6 and 0.7nm sample with temperature at 300-380 K and 150-300K, respectively.

Magnetic Structure Characterization. The variation in magnetic order of the $[Mn\ 0.7/Pt\ 0.1]_{20}$ film across different T_m was characterized using the resonant elastic x-ray scattering (REXS) technique. The REXS measurements were performed on the BL3A beamline at the KEK Photon Factory in Japan, utilizing the vertical scattering geometry on a four-circle diffractometer without an analyzer. Incident photon energies were selected via a silicon (111) monochromator, while the scattered photon intensity was detected using a silicon drift detector. First, the REXS intensity of the (0, 0, 1) peak was measured at 300 K as a function of incident photon energy near the Mn K edge. Second, rocking scans of the (0, 0, 1) peak of the $[Mn\ 0.7/Pt\ 0.1]_{20}$ film were performed as a function of T_m to monitor magnetic ordering of the Mn moments. These measurements were performed at incident photon energies close to the Mn K edge (E = 6.55 keV) to be sensitive to magnetic ordering, and with off-resonance measurements (E = 6.52 keV) taken for background comparison.

Density Functional Theory (DFT) calculation. The DFT calculations were performed using the VASP package,[38] which employs the projector-augmented wave (PAW) formalism to describe the wavefunctions, and we set the energy cutoff to 270 eV. The exchange-correlation functional was approximated using the PBE parameterization of the generalized gradient approximation (GGA).[39] Even though correlation effects beyond GGA are typically less important in metallic systems, it may still have some impact on Mn 3d orbitals due to their

localized nature, and this could be a topic for future investigation. The Brillouin zone was sampled with a maximum spacing of 0.15 $Å^{-1}$ and we kept the atoms in the original high symmetry sites as the atomic forces are zero by inversion symmetry. Also, spin-orbit coupling was incorporated in all calculations.

To evaluate the magnetic stability of the NCAF Mn_3Pt material, we rotated each spin within the Kagome plane away from the ground Γ_{10} symmetry state to Γ_7 symmetry state by 30°, 45°, 60°, and till 90° (Γ_7 state), while preserving their relative angles. The total energies were calculated for each of these configurations and these calculations were conducted for both cubic ($a = b = c$) and tetragonal ($a = b \neq c$) unit cells.

The anomalous Hall conductivity (AHC) of Mn_3Pt were calculated by using the Kubo formula,[48] with DFT eigenfunctions and eigenvalues as inputs. To ensure dense *k*-point sampling, the Wannier interpolation scheme[49] was employed to compute matrix elements efficiently, determining that a 100 x 100 x 100 *k*-grid provides sufficient convergence. The directions of the AHC tensor were defined using Cartesian axes x, y, and z, oriented along the crystallographic $[1\bar{1}0]$, $[11\bar{2}]$, [111] directions of the unit cell, respectively. In this framework, the x and y axes lie within the Kagome plane, while the z-axis is perpendicular to it.

Transport measurements. AHE measurements of the device samples were performed using a Quantum Design™ Physical Property Measurement System (PPMS) across T_m ranging from 50 to 400 K. For all device samples, a constant longitudinal current (I_{xx}) of 500 μA was applied along the *x*-direction (inset of Figure 3b). The Hall resistivity is calculated with the relation of $\rho_{xy} = \rho_{OHE} + \rho_{AHE} = \frac{V_{xy}}{I_{xx}} \cdot t_{Mn3Pt}$, where $\rho_{OHE/AHE}$, V_{xy} and t_{Mn3Pt} are the ordinary and anomalous Hall resistivity, the measured raw Hall voltage and film thickness of Mn_3Pt layer, respectively. The anomalous Hall resistivity loop was obtained by subtracting the OHE component from the Hall resistivity loop.[14]

Supporting Information

S1. Composition, morphology and magnetic properties of Mn_3Pt Layer.
S2. Crystallographic Texture.
S3. Group Theory Analysis.
S4. Anomalous Hall effect (AHE) Analysis.
S5. Density Functional Theory.
S6. Fitting of AHE Results.

Acknowledgements: We acknowledge experimental inputs from Lizhu Ren. This research is supported by the RIE2025 Manufacturing, Trade and Connectivity (MTC) Individual Research Grants (Grant No. M23M6c0101) and (Grant No. M24N7c0086), administered by A*STAR.

Conflict of Interest: All the authors have no conflicts of interest to disclose.

Data Availability: The data that support the findings of this study are available within the article.

References

[1] T. Jungwirth, X. Marti, P. Wadley, J. Wunderlich, *Nat. Nanotechnol.* **2016** 11 231-241.
[2] A. H. MacDonald, M. Tsoi, *Philos. Trans. R. Soc. A* **2011** 369 3098-3114.
[3] D.-F. Shao, E. Y. Tsymbal, *npj Spintronics* **2024** 2 13.

[4] S.-W. Cheong, F.-T. Huang, *npj quantum mater.* **2023** 8 73.
[5] S. Chen, D. J. X. Lin, B. C. Lim, P. Ho, *J. Phys. D: Appl. Phys.* **2024** 57 443001.
[6] M. T. Suzuki, T. Nomoto, R. Arita, Y. Yanagi, S. Hayami, H. Kusunose, *Phys. Rev. B* **2019** 99 174407.
[7] S. Nakatsuji, N. Kiyohara, T. Higo, *Nature* **2015** 527 212-215
[8] A. K. Nayak, J. E. Fischer, Y. Sun, B. Yan, J. Karel, A. C. Komarek, C. Shekhar, N. Kumar, W. Schnelle, J. Kubler, C. Felser, S. S. Parkin, *Sci Adv* **2016** 2 e1501870.
[9] H. Chen, Q. Niu, A. H. MacDonald, *Phys. Rev. Lett.* **2014** 112 017205.
[10] Y. Zhang, Y. Sun, H. Yang, J. Železný, S. P. P. Parkin, C. Felser, B. Yan, *Phys. Rev. B* **2017** 95 075128.
[11] L. Šmejkal, R. González-Hernández, T. Jungwirth, J. Sinova, *Sci. Adv.* **2020** 6 eaaz8809.
[12] J. Kübler, C. Felser, *Europhys. Lett.* **2014** 108 67001.
[13] L. Song, F. Zhou, H. Li, B. Ding, X. Li, X. Xi, Y. Yao, Y.-C. Lau, W. Wang, *Adv. Funct. Mater.* **2024** 34 2316588.
[14] S. Chen, D. J. X. Lin, B. C. Lim, H. K. Tan, Y. Y. K. Hnin, S. K. Wong, I. Lim, R. J. J. Lim, K. H. Khoo, P. Ho, *APL Mater.* **2023** 11 101126.
[15] P. J. Brown, V. Nunez, F. Tasset, J. B. Forsyth, P. Radhakrishna, *J. Phys.–Condens. Matter* **1990** 2 9409.
[16] P. Lukashev, R. F. Sabirianov, K. Belashchenko, *Phys. Rev. B* **2008** 78 184414.
[17] D.-F. Shao, G. Gurung, T. R. Paudel, E. Y. Tsymbal, *Phys. Rev. Mater.* **2019** 3 024405.
[18] H. Tsai, T. Higo, K. Kondou, T. Nomoto, A. Sakai, A. Kobayashi, T. Nakano, K. Yakushiji, R. Arita, S. Miwa, Y. Otani, S. Nakatsuji, *Nature* **2020** 580 608-613.
[19] T. Higo, K. Kondou, T. Nomoto, M. Shiga, S. Sakamoto, X. Chen, D. Nishio-Hamane, R. Arita, Y. Otani, S. Miwa, S. Nakatsuji, *Nature* **2022** 607 474-479.
[20] Y. Deng, X. Liu, Y. Chen, Z. Du, N. Jiang, C. Shen, E. Zhang, H. Zheng, H.-Z. Lu, K. Wang, *Natl. Sci. Rev.* **2022** 10 nwac154.
[21] J. Zelezny, Y. Zhang, C. Felser, B. Yan, *Phys Rev Lett* **2017** 119 187204.
[22] P. Qin, H. Yan, X. Wang, H. Chen, Z. Meng, J. Dong, M. Zhu, J. Cai, Z. Feng, X. Zhou, L. Liu, T. Zhang, Z. Zeng, J. Zhang, C. Jiang, Z. Liu, *Nature* **2023** 613 485-489.
[23] G. Gurung, D.-F. Shao, E. Y. Tsymbal, *Phys. Rev. Mater.* **2021** 5 124411.
[24] J. Shi, S. Arpaci, V. Lopez-Dominguez, V. K. Sangwan, F. Mahfouzi, J. Kim, J. G. Athas, M. Hamdi, C. Aygen, H. Arava, C. Phatak, M. Carpentieri, J. S. Jiang, M. A. Grayson, N. Kioussis, G. Finocchio, M. C. Hersam, P. Khalili Amiri, *Adv. Mater.* **2024** 36 2312008.
[25] S. Hu, C. Zheng, W. Fan, Y. Liu, *J. Magn. Magn. Mater.* **2023** 588 171393.
[26] V. Puliafito, R. Khymyn, M. Carpentieri, B. Azzerboni, V. Tiberkevich, A. Slavin, G. Finocchio, *Phys. Rev. B* **2019** 99 024405.
[27] T. Matsuda, T. Higo, T. Koretsune, N. Kanda, Y. Hirai, H. Peng, T. Matsuo, N. Yoshikawa, R. Shimano, S. Nakatsuji, R. Matsunaga, *Phys. Rev. Lett.* **2023** 130 126302.
[28] H. Bai, X. F. Zhou, H. W. Zhang, W. W. Kong, L. Y. Liao, X. Y. Feng, X. Z. Chen, Y. F. You, Y. J. Zhou, L. Han, W. X. Zhu, F. Pan, X. L. Fan, C. Song, *Phys. Rev. B* **2021** 104 104401.
[29] C. Cao, S. Chen, R.-C. Xiao, Z. Zhu, G. Yu, Y. Wang, X. Qiu, L. Liu, T. Zhao, D.-F. Shao, Y. Xu, J. Chen, Q. Zhan, *Nat. Commun.* **2023** 14 5873.
[30] H. Bai, Y. C. Zhang, L. Han, Y. J. Zhou, F. Pan, C. Song, *Appl. Phys. Rev.* **2022** 9 041316.
[31] Z. Q. Liu, H. Chen, J. M. Wang, J. H. Liu, K. Wang, Z. X. Feng, H. Yan, X. R. Wang, C. B. Jiang, J. M. D. Coey, A. H. MacDonald, *Nat. Electron.* **2018** 1 172-177.
[32] B. E. Zuniga-Cespedes, K. Manna, H. M. L. Noad, P.-Y. Yang, M. Nicklas, C. Felser, A. P. Mackenzie, C. W. Hicks, *New J. Phys.* **2023** 25 023029.
[33] E. Krén, G. Kádár, L. Pál, J. Sólyom, P. Szabó, *Phys. Lett.* **1966** 20 331-332.
[34] E. Krén, G. Kádár, L. Pál, P. Szabó, *J. Appl. Phys.* **1967** 38 1265-1266.
[35] J. Kubler, K. H. Hock, J. Sticht, A. R. Williams, *J. Phys. F* **1988** 18 469.

[36] J. Mukherjee, T. S. Suraj, H. Basumatary, K. Sethupathi, K. V. Raman, *Phys. Rev. Mater.* **2021** 5 014201.
[37] S. Xu, B. Dai, Y. Jiang, D. Xiong, H. Cheng, L. Tai, M. Tang, Y. Sun, Y. He, B. Yang, Y. Peng, K. L. Wang, W. Zhao, *Nat Commun* **2024** 15 3717.
[38] G. Kresse, J. Furthmüller, *Phys. Rev. B* **1996** 54 11169-11186.
[39] J. P. Perdew, K. Burke, M. Ernzerhof, *Phys. Rev. Lett.* **1996** 77 3865-3868.
[40] P. F. Ladwig, Y. A. Chang, E. S. Linville, A. Morrone, J. Gao, B. B. Pant, A. E. Schlutz, S. Mao, *J. Appl. Phys.* **2003** 94 979-987.
[41] I. Opahle, H. K. Singh, J. Zemen, O. Gutfleisch, H. Zhang, *Phys. Rev. Res.* **2020** 2 023134
[42] N. An, M. Tang, S. Hu, H. Yang, W. Fan, S. Zhou, X. Qiu, *SCI CHINA PHYS MECH* **2020** 63 297511.
[43] O. V. Kovalev, A. M. Gross, *Irreducible representations of the space groups* Gordon and Breach: New York, 1965.
[44] S. C. Miller, W. F. Love, *Tables of irreducible representations of space groups and co-representations of magnetic space groups* Pruett, Boulder, 1967.
[45] S. Deng, H. Wang, L. He, C. Wang, *Microstructure* **2023** 3 2023044.
[46] P. Roy, D. Zhang, A. R. Mazza, N. Cucciniello, S. Kunwar, H. Zeng, A. Chen, Q. Jia, *Nanoscale* **2023** 15 17589-17598.
[47] D. Torres-Amaris, A. Bautista-Hernandez, R. González-Hernández, A. H. Romero, A. C. Garcia-Castro, *Phys. Rev. B* **2022** 106 195113.
[48] N. Nagaosa, J. Sinova, S. Onoda, A. H. MacDonald, N. P. Ong, *Rev. Mod. Phys.* **2010** 82 1539-1592.
[49] G. Pizzi, V. Vitale, R. Arita, S. Blügel, F. Freimuth, G. Géranton, M. Gibertini, D. Gresch, C. Johnson, T. Koretsune, J. Ibañez-Azpiroz, H. Lee, J.-M. Lihm, D. Marchand, A. Marrazzo, Y. Mokrousov, J. I. Mustafa, Y. Nohara, Y. Nomura, L. Paulatto, S. Poncé, T. Ponweiser, J. Qiao, F. Thöle, S. S. Tsirkin, M. Wierzbowska, N. Marzari, D. Vanderbilt, I. Souza, A. A. Mostofi, J. R. Yates, *J. Phys.–Condens. Matter* **2020** 32 165902.
[50] S. Onoda, N. Sugimoto, N. Nagaosa, *Phys. Rev. B* **2008** 77 165103.
[51] X. Chen, X. Zhang, M.-G. Han, L. Zhang, Y. Zhu, X. Xu, X. Hong, *Adv. Mater.* **2019** 31 1805260.
[52] D. Yue, X. Jin, *Journal of the Physical Society of Japan* **2017** 86 011006.
[53] W. Zhang, W. Han, S.-H. Yang, Y. Sun, Y. Zhang, B. Yan, S. S. P. Parkin, *Sci. Adv.* **2016** 2 e1600759.
[54] P. K. Muduli, T. Higo, T. Nishikawa, D. Qu, H. Isshiki, K. Kondou, D. Nishio-Hamane, S. Nakatsuji, Y. Otani, *Phys. Rev. B* **2019** 99 184425.
[55] G.-Y. Guo, T.-C. Wang, *Phys. Rev. B* **2017** 96 224415.
[56] M. Ikhlas, T. Tomita, T. Koretsune, M.-T. Suzuki, D. Nishio-Hamane, R. Arita, Y. Otani, S. Nakatsuji, *Nat. Phys.* **2017** 13 1085-1090.
[57] X. Li, L. Xu, L. Ding, J. Wang, M. Shen, X. Lu, Z. Zhu, K. Behnia, *Phys. Rev. Lett.* **2017** 119 056601.
[58] H. Narita, M. Ikhlas, M. Kimata, A. A. Nugroho, S. Nakatsuji, Y. Otani, *Appl. Phys. Lett.* **2017** 111 202404
[59] S. Y. Bodnar, M. Filianina, S. P. Bommanaboyena, T. Forrest, F. Maccherozzi, A. A. Sapozhnik, Y. Skourski, M. Kläui, M. Jourdan, *Phys. Rev. B* **2019** 99 140409.
[60] T. Higo, H. Man, D. B. Gopman, L. Wu, T. Koretsune, O. M. J. van 't Erve, Y. P. Kabanov, D. Rees, Y. Li, M. T. Suzuki, S. Patankar, M. Ikhlas, C. L. Chien, R. Arita, R. D. Shull, J. Orenstein, S. Nakatsuji, *Nat Photonics* **2018** 12 73-78.
[61] S. M. Rezende, A. Azevedo, R. L. Rodríguez-Suárez, *J. Appl. Phys.* **2019** 126 151101
[62] M. Kimata, N. Sasabe, K. Kurita, Y. Yamasaki, C. Tabata, Y. Yokoyama, Y. Kotani, M. Ikhlas, T. Tomita, K. Amemiya, H. Nojiri, S. Nakatsuji, T. Koretsune, H. Nakao, T.-h. Arima, T. Nakamura, *Nat. Commun.* **2021** 12 5582.

[63] X. Chen, T. Higo, K. Tanaka, T. Nomoto, H. Tsai, H. Idzuchi, M. Shiga, S. Sakamoto, R. Ando, H. Kosaki, T. Matsuo, D. Nishio-Hamane, R. Arita, S. Miwa, S. Nakatsuji, *Nature* **2023** 613 490-495.
[64] W.-B. Lee, S. Hwang, H.-W. Ko, B.-G. Park, K.-J. Lee, G.-M. Choi, *Nat. Nanotechnol.* **2025** 20 487-493.
[65] Y. Takeuchi, Y. Yamane, J.-Y. Yoon, R. Itoh, B. Jinnai, S. Kanai, J. i. Ieda, S. Fukami, H. Ohno, *Nat. Mater.* **2021** 20 1364-1370.
[66] P. Rzeszut, J. Chęciński, I. Brzozowski, S. Ziętek, W. Skowroński, T. Stobiecki, *Sci. Rep.* **2022** 12 7178.
[67] A. Kumar, D. J. X. Lin, D. Das, L. Huang, S. L. K. Yap, H. R. Tan, H. K. Tan, R. J. J. Lim, Y. T. Toh, S. Chen, S. T. Lim, X. Fong, P. Ho, *ACS Appl. Mater. Interfaces.* **2024** 16 10335-10343.

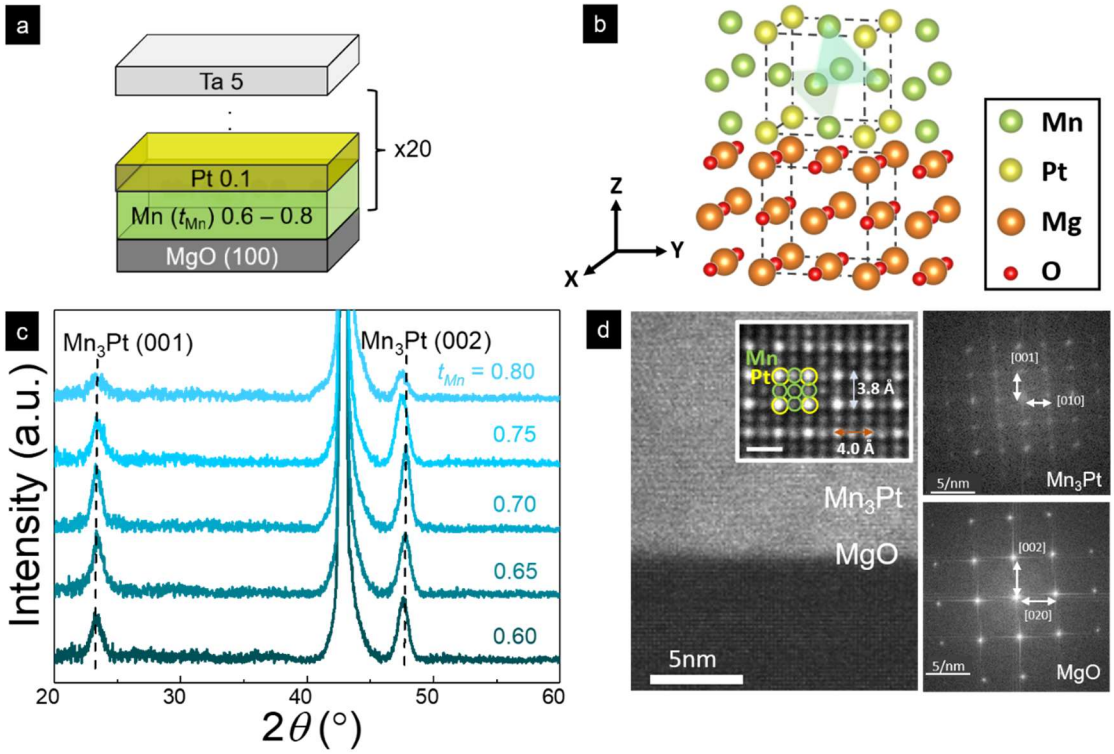

Figure 1. Schematic of Mn3Pt multilayer and XRD and TEM results of corresponding samples. (a) Schematic of noncollinear antiferromagnetic (NCAF) $[Mn/Pt]_{20}$ multilayer deposited on single crystal MgO (001) substrate. The Mn layer thickness (t_{Mn}) is varied from 0.6 – 0.8 nm while the Pt layer is fixed at 0.1 nm. (b) Schematic of the epitaxial growth of Mn_3Pt (001) on MgO (001) lattice. The Kagome plane of the Mn_3Pt lattice is stacked along the [111] direction. (c) XRD spectra of the Mn_3Pt multilayers across varying t_{Mn} of 0.6 – 0.8 nm. (d) High-angle annular dark-field scanning transmission electron microscopy (HAADF-STEM) image of a cross-sectional MgO/Mn_3Pt for t_{Mn}: 0.7 nm. Inset is an atomic resolution image confirming the $L1_2$ Mn_3Pt structure, where green and yellow circles indicate the Mn and Pt atom position, respectively, and an in-plane and out-of-plane interlayer spacing of 4.0 and 3.80 Å (scale bar: 5 nm), respectively. Corresponding fast Fourier transform images (scale bar: 5/nm) affirm the epitaxial growth of Mn_3Pt on MgO along the (001) direction.

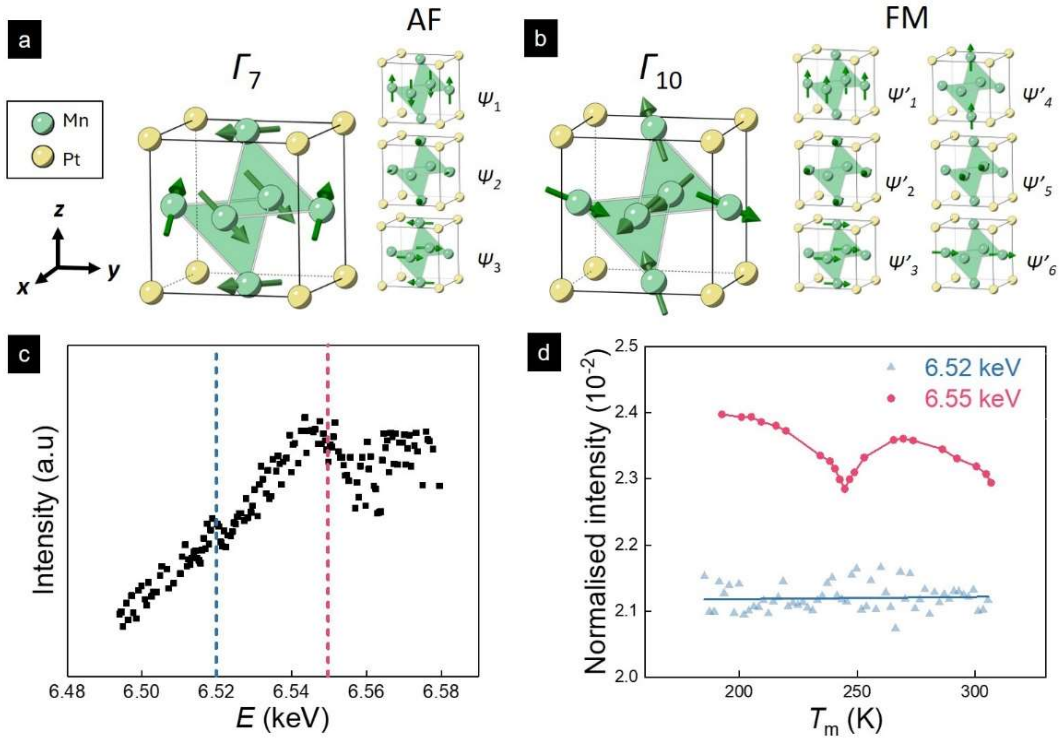

Figure 2. Schematic of $L1_2$ Mn_3Pt magnetic structure and REXS measurement results. (a-b) Schematic of Mn_3Pt with (a) Γ_7 (left) and (b) Γ_{10} (left) magnetic structure. The Γ_7 magnetic structure is described by three antiferromagnetic basis vectors (ψ_1, ψ_2, ψ_3) (right), while the Γ_{10} magnetic structure is described by six ferromagnetic basis vectors (ψ'_1, ψ'_2, ψ'_3, ψ'_4, ψ'_5, ψ'_6) (right). (c-d) Resonant elastic x-ray scattering measurements of the t_{Mn} = 0.7 nm Mn_3Pt multilayer. (c) Photon energy dependence of the (001) reflection at T_m = 300 K. (d) Temperature (T_m) dependence of the (001) peak measured at fixed photon energies of 6.52 or 6.55 keV.

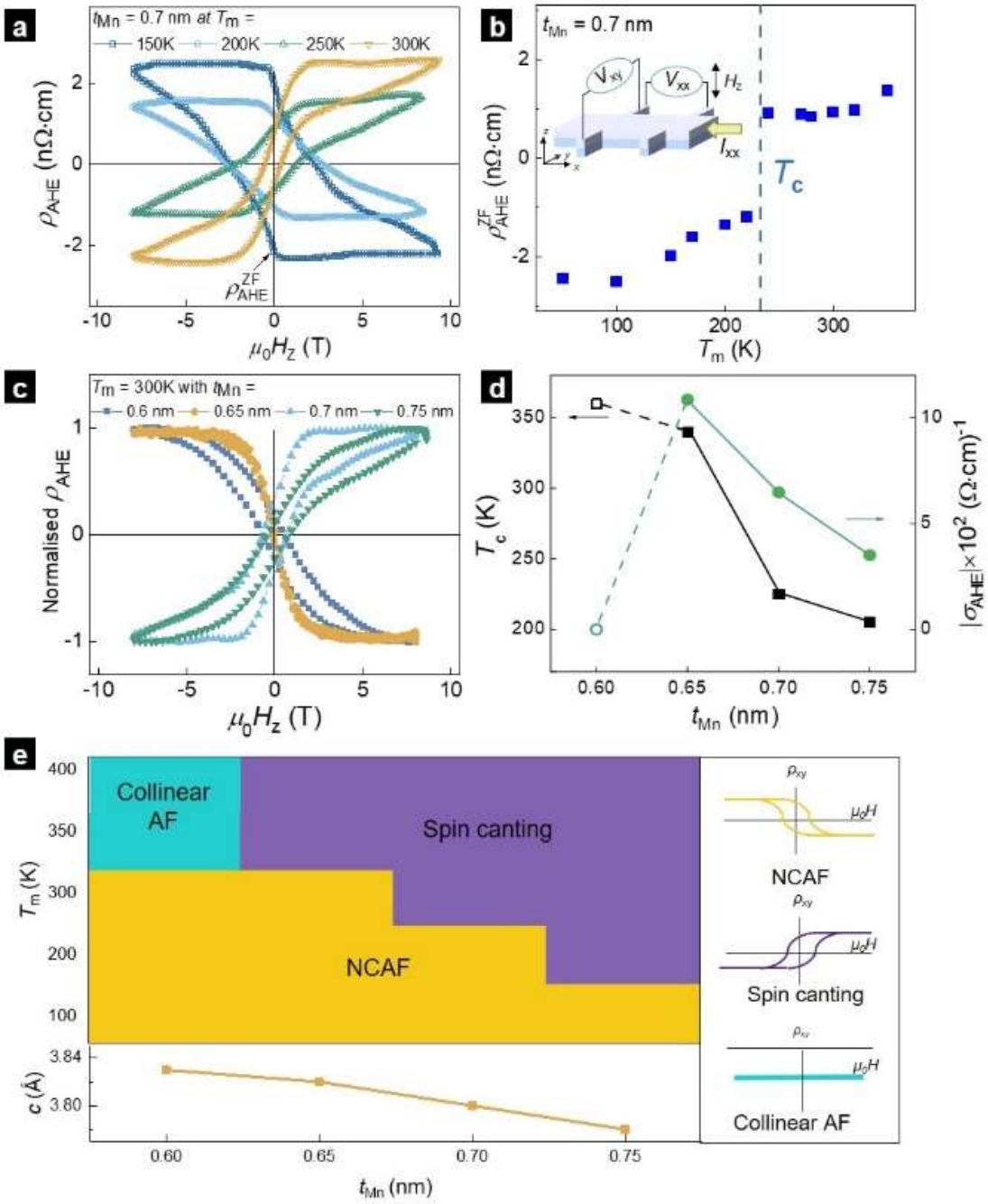

Figure 3. AHE measurement results. (a) Anomalous Hall resistivity (ρ_{AHE}) as a function of out-of-plane magnetic field ($\mu_0 H_Z$) across a range of T_m = 150 − 300 K for the t_{Mn} = 0.7 nm Mn_3Pt Hall bar device (schematic in (b) inset) (b) Zero-field anomalous Hall resistivity (ρ_{AHE}^{ZF}, indicated in (a)) of the t_{Mn} = 0.7 nm Mn_3Pt device acquired across varying T_m = 50 − 300 K. The critical temperature T_c (dotted line) indicates a reversal in sign of the ρ_{AHE}^{ZF}. (c) The normalized ρ_{AHE} versus $\mu_0 H_Z$ loops measured at T_m = 300 K for t_{Mn}=0.6 − 0.75 nm Mn_3Pt Hall bar devices. (d) Surmised T_c (black line) and ρ_{AHE}^{ZF} (green line) for t_{Mn} = 0.6 − 0.75 nm Mn_3Pt Hall devices. (e) Colour plot representation of the evolution of AHE loop polarity (left, top) and corresponding magnetic order (right) of the t_{Mn}=0.6−0.75 nm Mn_3Pt devices across varying T_m = 50 − 300 K. Bottom left plot shows the variation of room-temperature lattice constant c across the t_{Mn} = 0.6 − 0.75 nm Mn_3Pt devices.

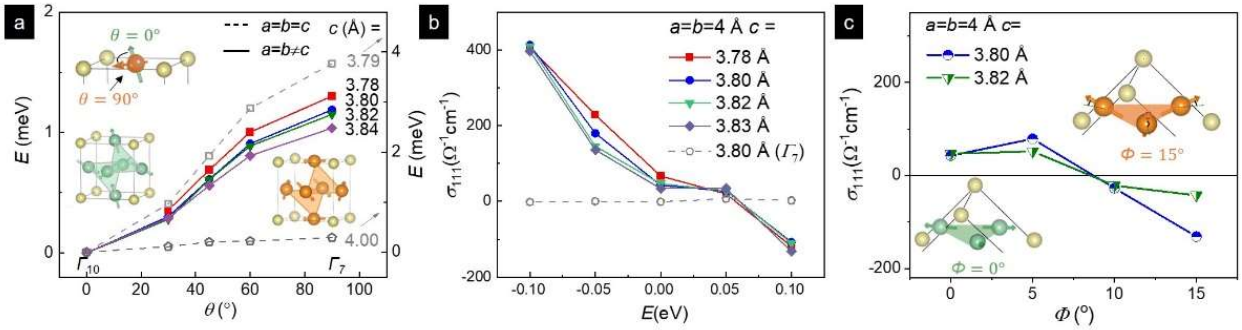

Figure 4. DFT calculation results. (a) Total energy of the magnetic states as a function of changing rotation angles θ relative to the Γ_{10} symmetry ground state (θ = 0°), while preserving the relative angles of the three spins within the Kagome plane at 120°. The total energy is calculated for cubic ($a = b = c$, dotted lines) and tetragonal unit cell ($a = b \neq c$, solid lines) (b) Calculated anomalous Hall conductivity along the Kagome plane (σ_{111}) as a function of Fermi energy shift for the Γ_{10} symmetry ground state with lattice constants 4.0 × 4.0 × 3.78 - 3.83 Å (solid lines), and the Γ_7 symmetry state for 4.0 × 4.0 × 3.80 Å (dotted line). (c) σ_{111} as a function of Fermi energy shift for the 4.0 × 4.0 × 3.80 and 4.0 × 4.0 × 3.82 Å crystal lattices where the spins of the Γ_{10} magnetic structure are tilted out of the Kagome plane by fixed angles of Φ ranging from 0 – 15°.

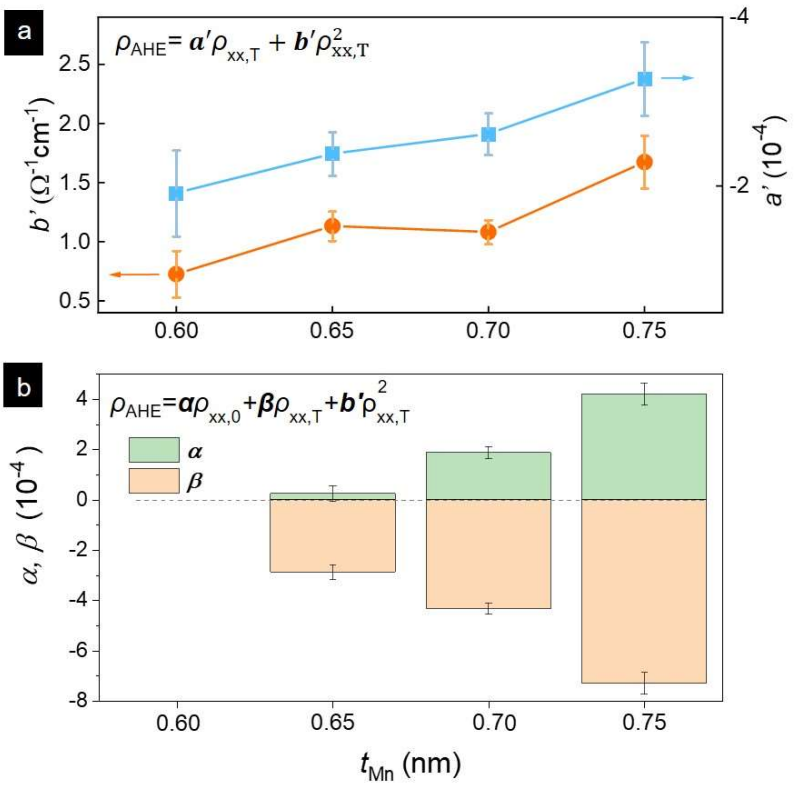

Figure 5. Fitting parameters of AHE results. (a) Fitting parameters ***a'*** and ***b'*** derived from the AF scaling law ($\rho_{AHE} = \boldsymbol{a}'\rho_{xx,T} + \boldsymbol{b}'\rho_{xx,T}^2$) and (b) $\boldsymbol{\alpha}$ and $\boldsymbol{\beta}$ derived from the FM scaling law ($\rho_{AHE} = \boldsymbol{\alpha}\rho_{xx,0} + \boldsymbol{\beta}\rho_{xx,T} + \boldsymbol{b}'\rho_{xx,T}^2$).

Supporting Information

Tailoring antiferromagnetic orders and spin transport in noncollinear Mn_3Pt multilayers

Shaohai Chen[1]†, Bee Chun Lim[1]†, Dennis J. X. Lin[1]†, Jian Rui Soh[2], Hui Ru Tan[1], Hang Khume Tan[1], Hnin Yu Yu Ko[1], Seng Kai Wong[1], Mingsheng Zhang[1], Robert Laskowski[3], Tieyang Zhao[4], Jingsheng Chen[4], Khoong Hong Khoo[3], Pin Ho[1]**

Contents

S1. Composition, Mophology and Magnetic Properties of Mn_3Pt Layer

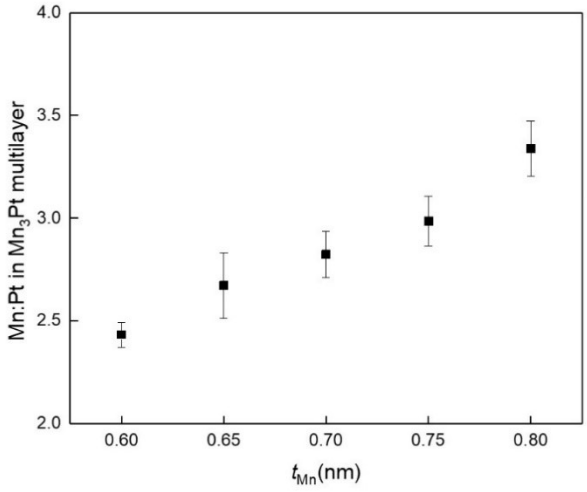

Figure. S1. Atomic percentage ratio of Mn to Pt in the Mn_3Pt multilayers with varying Mn thickness, t_{Mn} = 0.6 – 0.8 nm.

Atomic percentage of Mn_3Pt multilayers with t_{Mn}=0.6-0.8 nm. Atomic percentages of Mn and Pt were determined using the x-ray photoelectron spectroscopy (XPS) depth profile technique. The Mn:Pt atomic ratio of the samples were measured from the depth profile spectra acquired after ~300s of sputtering to ensure exclusion of surface oxidation and contaminants from compositional analysis.

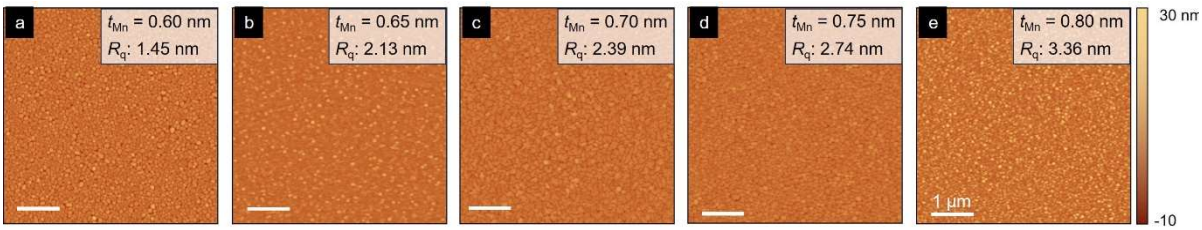

Figure. S2. (a-e) Atomic force microscopy (AFM) images (scale bar: 1 µm) of the MgO/Mn_3Pt/Ta samples across varying t_{Mn} = 0.6-0.8 nm, respectively.

Mophology of Mn_3Pt multilayers with t_{Mn}=0.6-0.8 nm: Atomic force microscopy (AFM) measurements were performed to characterize the surface morphology of the sample with t_{Mn} = 0.6-0.8 nm (Figure S2). The measured root-mean-square (RMS, R_q) roughness from 1.45 to 3.36 nm with increasingly thicker t_{Mn} from 0.6 to 0.75 nm (Fig. S2). All samples exhibit a granular surface structure, consistent with the island-like growth mechanism of thin film under high deposition temperature conditions i.e. T_s ~500 °C and lattice mismatch between the Mn_3Pt film and MgO(001) substrate i.e. ~9%.

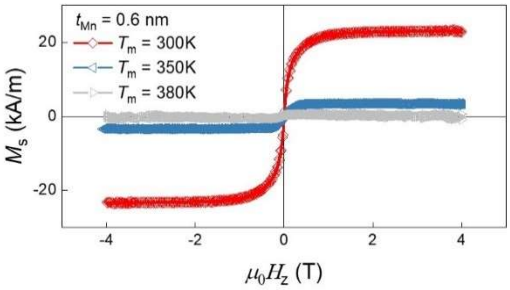

Figure. S3-1. Magnetic hysteresis (*M-H*) loops as a function of out-of-plane magnetic field ($\mu_0 H_Z$) across a range of T_m = 300 − 380 K for the t_{Mn} = 0.6 nm Mn_3Pt film.

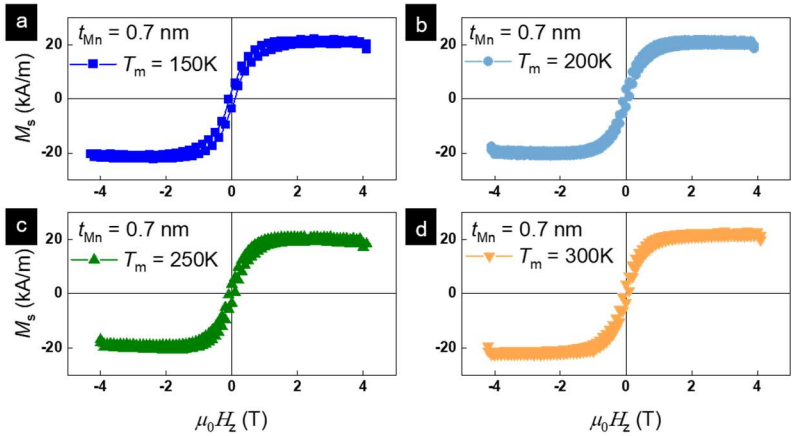

Figure. S3-2. Magnetic hysteresis (*M-H*) loops as a function of out-of-plane magnetic field ($\mu_0 H_Z$) across a range of T_m = 150 − 300 K for the t_{Mn} = 0.7 nm Mn_3Pt film.

Magnetic hysteresis loops of the t_{Mn}= 0.6 and 0.7 nm sample across varying T_m: We performed the temperature-dependent *M-H* loops of the t_{Mn} = 0.6 and 0.7 nm samples at T_m = 300 – 380 K and 150-300 K, respectively. The out-of-plane (OP) magnetic hysteresis (*M-H*) loops of the t_{Mn}= 0.6 nm sample show a rapid suppression of magnetization at $T_m \geq 350$ K (Figure S3-1). This indicates that Mn_3Pt undergoes a first-order magnetic phase transition from a low-temperature NCAF to a high-temperature collinear AF magnetic structure.
Additionally, the OP *M-H* loops of the t_{Mn}= 0.7 nm sample across varying T_m = 100 - 300K (Figure S3-2) are continuous with no step-like features, indicating coherent switching typical of a single magnetic phase. In comparison with the AHE loops of similar T_m (Fig. 3a), we note that the coercive fields of the AHE loops are significantly larger than the corresponding *M–H* loops. Such discrepancy was also reported by Xu *et al.* [31]. We ascribe the difference to the distinct physical origins contributing to hysteresis in the two characterization techniques. In the *M–H* measurement, the external OP magnetic field induces a tilt of the antiferromagnetic spin structure along the applied field direction, while the vanishingly small remanent moment at zero field reflects the intrinsic canted spin arrangement. In contrast, the larger coercive fields observed in the AHE loops point to additional contributions from spin transport mechanisms – mainly originating from the nonvanishing Berry curvature and nontrivial band topology, rather than being solely governed by magnetic moment reversal. Expectedly, the coercive fields in the AHE loop will not directly correlate with those in the *M–H* loops.

S2. Crystallographic Texture

Lattice constant and crystallinity: Based on the x-ray diffraction (XRD) spectrum, the lattice constant, c, was determined using Bragg's Law, $n\lambda = 2d_{hkl}\sin\theta$, where n, λ (=1.54 Å), d_{hkl} and θ is the reflection order, x-ray wavelength, interplanar spacing and diffraction angle in radians, respectively. The lattice constant c (= d_{001}), corresponding to the Mn_3Pt (001) peak θ_{001}, is calculated for the t_{Mn} = 0.6-0.8 nm multilayers and summarized in Table S1. Meanwhile, the full width at half maximum (FWHM) for the 5 multilayer stacks is summarized in Table S2.

Table S1. Parameters calculated from the Mn_3Pt (001) diffraction peak of the t_{Mn}= 0.6 – 0.8 nm multilayers.

t_{Mn} (nm)	2θ (°)	θ (rad)	d_{001} (Å)	c (Å)
0.60	23.18	0.20	3.83	3.83
0.65	23.28	0.20	3.82	3.82
0.70	23.38	0.20	3.80	3.80
0.75	23.54	0.21	3.78	3.78
0.80	23.20	0.20	3.83	3.83

Table S2. Full width at half maximum (FWHM) for the Mn_3Pt (001) and (002) peaks of the t_{Mn}= 0.6 – 0.8 nm multilayers.

t_{Mn} (nm)	FWHM (°)	
	(001)	(002)
0.60	1.176	0.984
0.65	0.959	0.945
0.70	0.923	0.901
0.75	1.108	1.112
0.80	2.055	1.091

S3. Group Theory Analysis

Basis vectors of Mn_3Pt magnetic structure with Γ_7 and Γ_{10} symmetry: Given that the Mn atom resides on the *3c* Wyckoff position of cubic $Pm\bar{3}m$ (#221) space group, the symmetry-allowed magnetic structure of $L1_2$ Mn_3Pt exists in terms of two irreducible representations, namely Γ_7 and Γ_{10} symmetry[43, 44], and in some instances termed as T_1 and T_2, (B) and (A), or Γ^{4g} and Γ^{5g},[33-35, 45] respectively. Utilizing group theory analysis, we observed that the Γ_7 and Γ_{10} magnetic structures display three antiferromagnetic ($\psi_{1\text{-}3}$) and six ferromagnetic ($\psi_{1'\text{-}6'}$) basis vectors respectively. The full 9 degrees of freedom of the magnetic order on the three Mn sites (***r***) of these basis vectors are tabulated in Table S3. Based on the basis vectors, the net magnetic moments can be described as $\boldsymbol{M}(\Gamma_7) \propto \sum_{i=1-3} C_i \boldsymbol{\psi}_i$ and $\boldsymbol{M}(\Gamma_{10}) \propto \sum_{i'=1-6} C_{i'} \boldsymbol{\psi}_{i'}$, respectively, where C_i and $C_{i'}$ are coefficient corresponding to a specific Kagome plane. In particular, for the case with the magnetic moment of Mn aligned in the (111) Kagome plane, it can be expressed as $\boldsymbol{M}(\Gamma_7) \propto (\boldsymbol{\psi_1} + \boldsymbol{\psi_2} + \boldsymbol{\psi_3})$ and $\boldsymbol{M}(\Gamma_{10}) \propto (-\boldsymbol{\psi'_1} - \boldsymbol{\psi'_2} - \boldsymbol{\psi'_3} + 2\boldsymbol{\psi'_4} + 2\boldsymbol{\psi'_5} + 2\boldsymbol{\psi'_6})$, respectively.

Table S3. Positions of *3c* Wyckoff site of Mn and magnetic moment orientation of the basis vectors, $\psi_{1\text{-}3}$ *and* $\psi'_{1\text{-}6}$, constituting the Γ_7 and Γ_{10} magnetic structures, respectively.

3c Wyckoff site of Mn, $\boldsymbol{r} = (x\ y\ z)$			(0 ½ 0)	(½ 0 ½)	(½ ½ 0)
Magnetic moment orientation, $\boldsymbol{M} = (m_x, m_y, m_z)$	Γ_7	ψ_1	(0,0,1)	(0,0,-1)	(0,0,0)
		ψ_2	(0,0,0)	(1,0,0)	(-1,0,0)
		ψ_3	(0,-1,0)	(0,0,0)	(0,1,0)
	Γ_{10}	Ψ'_1	(0,0,1)	(0,0,1)	(0,0,0)
		Ψ'_2	(0,0,0)	(1,0,0)	(1,0,0)
		Ψ'_3	(0,1,0)	(0,0,0)	(0,1,0)
		Ψ'_4	(0,0,0)	(0,0,0)	(0,0,1)
		Ψ'_5	(1,0,0)	(0,0,0)	(0,0,0)
		Ψ'_6	(0,0,0)	(0,1,0)	(0,0,0)

S4. Anomalous Hall Effect (AHE) Analysis

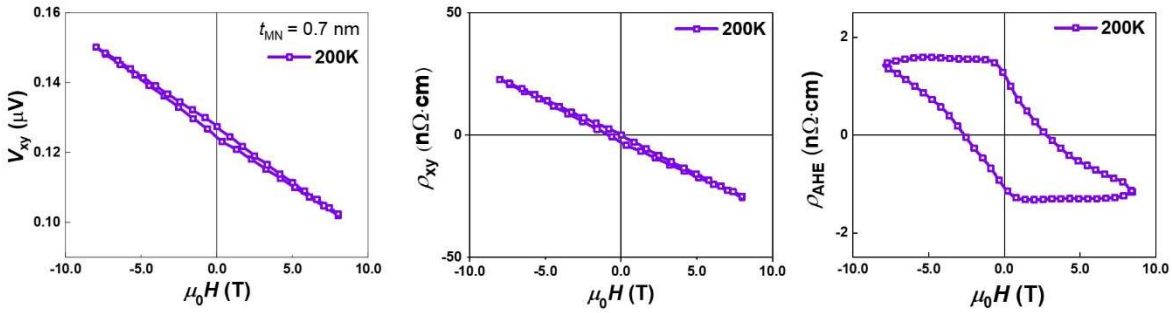

Figure. S4. Data processing procedure performed on the Hall measurements. (a) A representative as-acquired Hall voltage plot, V_{xy} vs. $\mu_0 H$, at 200 K. (b) The corresponding symmetrized Hall resistivity loop (ρ_{xy} vs. $\mu_0 H$) after removing the arbitrary offset imposed by PPMS. (c) Anomalous Hall resistivity loop (ρ_{AHE} vs. $\mu_0 H$) upon subtracting the ordinary Hall effect component.

Deriving AHE loops: Figure S4 shows the data processing procedure performed on the Hall measurement data acquired for the representative t_{Mn}=0.7 nm multilayer at measurement temperature T_m = 200 K. The raw Hall resistivity data of the sample was first corrected to eliminate offsets caused by electrode misalignment (Figure. S4a, b). Subsequently, the ordinary Hall effect (OHE) component was subtracted from the corrected Hall resistivity loop, thereby isolating the contribution arising from the AHE (Figure. S4b, c).

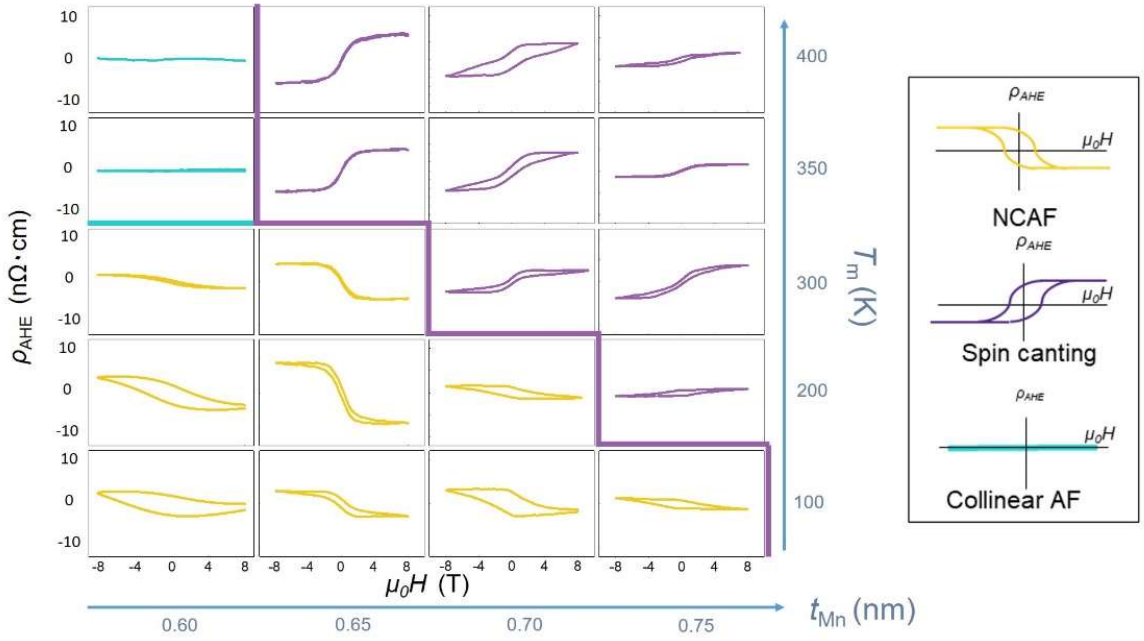

Figure. S5. Evolution of AHE loop polarity of the t_{Mn}=0.6−0.75 nm Mn_3Pt devices across varying T_m = 50 − 300 K. The yellow, purple and cyan color represents the AHE loops with negative, positive and no polarity, respectively - corresponding to NCAF, spin canting and collinear AF magnetic order.

AHE loops of t_{Mn} = 0.6 - 0.75 nm multilayers across varying T_m: The Hall data processing procedure was applied to all the measurements acquired for the t_{Mn} = 0.6 - 0.75 nm multilayers across varying T_m = 100 – 400 K (Figure S5). These are represented in the colour plot in main

manuscript Figure 3e to concisely depict the t_{Mn}– and T_m–dependence of AHE polarity and magnetic structures.

S5. Density Functional Theory

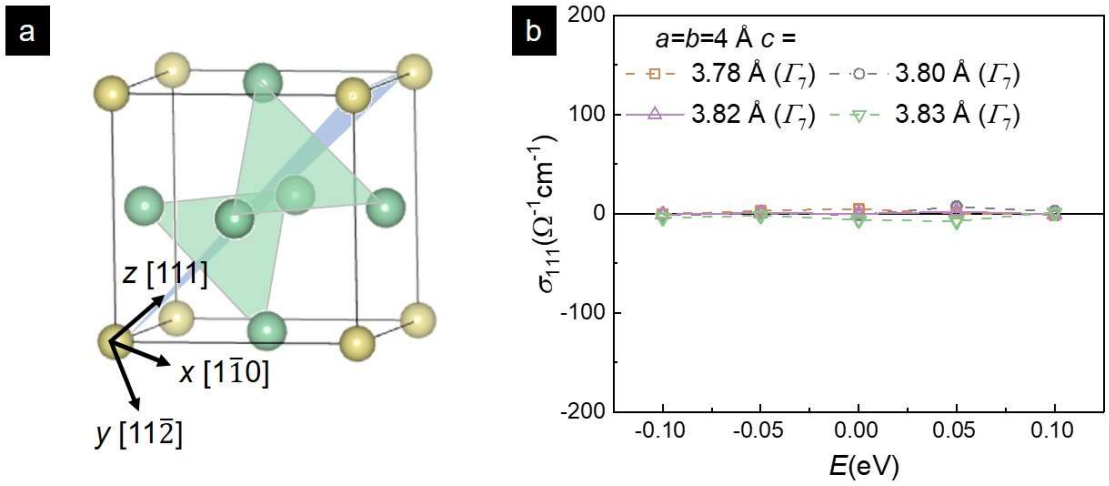

Figure S6. AHC of the Γ_7 magnetic structure with different lattice constant *c*. (a) Schematic of the Mn_3Pt lattice with *x*, *y*, *z* directions defined as [1$\bar{1}$0], [11$\bar{2}$] and [111], respectively. (b) Calculated anomalous Hall conductivity (AHC) along the Kagome plane (σ_{111}) as a function of Fermi energy shift for the Γ_7 symmetry ground state with lattice constants 4.0 × 4.0 × 3.78~3.83 Å.

AHC of the Γ_7 magnetic structure with different lattice constant c: In the DFT calculations, the directions of the anomalous Hall conductivity (AHC) tensor were redefined using the Cartesian coordinate system (x,y,z), which were aligned with the crystallographic [1$\bar{1}$0], [11$\bar{2}$] and [111] directions of the unit cell, respectively (Figure S6a). For Mn_3Pt with the Γ_7 magnetic structure, the calculations indicate that varying the lattice constant *c* within the range of 3.78~3.83 Å has no significant effect on σ_{111} (Figure S6b).

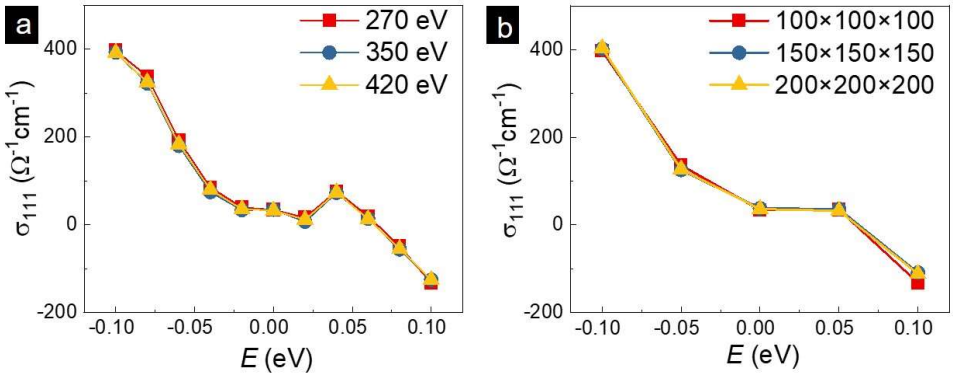

Figure S7. AHC of the Γ_{10} magnetic structure with different (a) energy cut-off values and (b) *k*-meshes.

AHC of the Γ_{10} magnetic structure with different energy cut-off values and k-meshes: A convergence test is performed to validate the choice of energy cutoff value of 270 eV used in our calculations. The AHC results for the 4.0×4.0×3.83 Å system with the Γ_{10} magnetic configuration show convergence to within 5 $W^{-1}cm^{-1}$ at 270 eV, which is sufficient for our purposes. (Figure S7a) Similarly, we validated that the *k*-mesh used is well-converged. Keeping the energy cutoff fixed at 270 eV, the AHC for the 4.0×4.0×3.83 Å system with the Γ_{10}

magnetic configuration shows good convergence to within ± 5 $W^{-1}cm^{-1}$ at 100×100×100 *k*-mesh, which is sufficiently accurate this work. (Figure S7b)

S6. Fitting of AHE Results

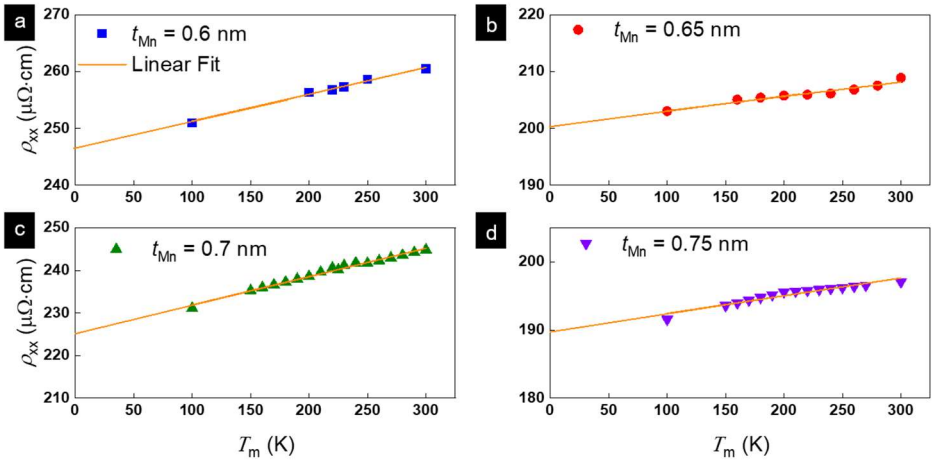

Figure S8. The longitudinal resistivity variations on measuring temperature ranging from 300 to 100K of the samples with (a)-(d) t_{Mn} = 0.6 - 0.75 nm, respectively.

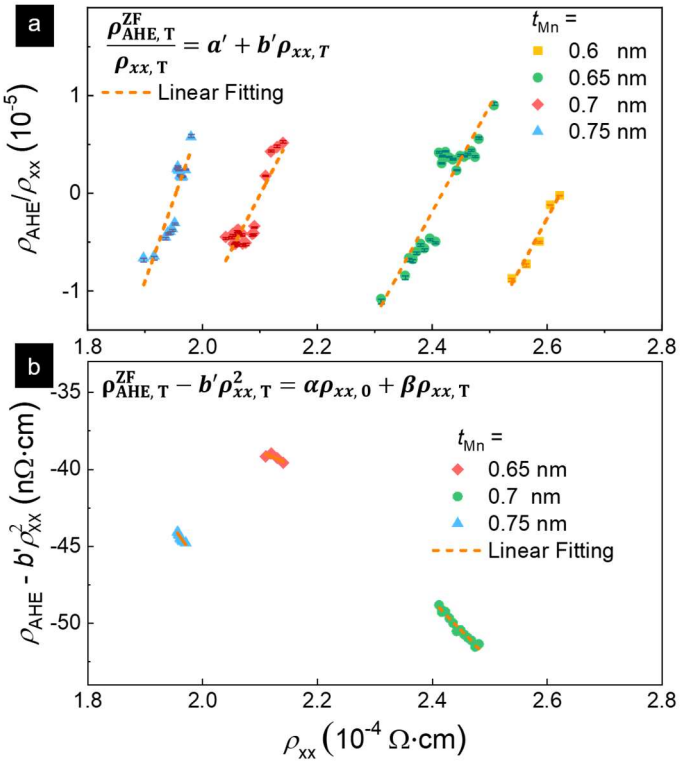

Figure S9. Fitting of AHE Results. (a-b) Fitting of the AHE data to determine the extrinsic and intrinsic contributions for t_{Mn} = 0.60 - 0.75 nm multilayers by using the (a) antiferromagnetic and (b) ferromagnetic scaling law.

Table S4. Summary of $\rho_{xx}(0)$ used in the FM scaling law fit and goodness of fit, R^2 of the two fitting possesses

t_{Mn} (nm)	$\rho_{xx,0}$(mΩ·cm)	R^2	
		AF scaling law	FM scaling law
0.60	0.246	0. 958	-

0.65	0.199	0.816	0.657
0.70	0.226	0.843	0.968
0.75	0.189	0.799	0.924

Determining the AHE signal contributions: The $\rho_{\mathrm{AHE,T}}^{\mathrm{ZF}}$ data of the t_{Mn} = 0.60 – 0.75 nm Mn_3Pt multilayers acquired across varying T_{m} = 100 – 400 K are linear fitted with the antiferromagnetic (AF) scaling law, $\frac{\rho_{\mathrm{AHE,T}}^{\mathrm{ZF}}}{\boldsymbol{\rho_{\mathrm{xx,T}}}} = \boldsymbol{a'} + \boldsymbol{b'\rho_{\mathrm{xx,T}}}$ (Figure S9a). For the t_{Mn} = 0.65 – 0.75 nm samples which exhibit positive AHE polarity, the $\rho_{\mathrm{AHE,T}}^{\mathrm{ZF}}$ data are further fitted using the modified ferromagnetic (FM) scaling law, $\rho_{\mathrm{AHE,T}}^{\mathrm{ZF}} - \boldsymbol{b'}\rho_{\mathrm{xx,T}}^{2} = \boldsymbol{\alpha}\rho_{\mathrm{xx,0}} + \boldsymbol{\beta}\rho_{\mathrm{xx,T}}$, whilst incorporating the fitting parameter $\boldsymbol{b'}$ obtained from AF scaling law (Figure S9b). The values of $\rho_{\mathrm{xx,0}}$ are acquired from the $\rho_{\mathrm{xx,T}}$ vs. T_{m} plot by linearly extrapolating to 0 K (Figure S8). Table S4 shows the goodness of fit, R^2, of the two fitting processes and the $\rho_{\mathrm{xx,T}}$ of t_{Mn} = 0.60 – 0.75 nm samples, respectively.